

Article

Microstructure, Mechanical Properties and Fracture Behavior of Micron-Sized TiB₂/AlZnMgCu(Sc,Zr) Composites Fabricated by Selective Laser Melting

Peng Yin ^{1,2,3} , Yantao Liu ^{1,2,3}, Zhuoheng Liang ^{1,2,3}, Wei Pan ^{1,2,3}, Shuobing Shao ^{1,2,3} and Yongzhong Zhang ^{1,2,3,*}

- ¹ National Engineering & Technology Research Center for Non-Ferrous Metals Composites, GRINM Group Corporation Limited, Beijing 101407, China
² Grinm Metal Composites Technology Co., Ltd., Beijing 101407, China
³ General Research Institute for Nonferrous Metals, Beijing 100088, China
* Correspondence: yzhang@grinm.com; Tel.: +86-13501008631

Abstract: In this paper, micron-sized TiB₂/AlZnMgCu(Sc,Zr) composites were fabricated by selective laser melting (SLM) using directly mixed powder. Nearly fully dense (over 99.5%) and crack-free SLM-fabricated TiB₂/AlZnMgCu(Sc,Zr) composite samples were obtained and its microstructure and mechanical properties were investigated. It is found that the laser absorption rate of powder is improved by introducing micron-sized TiB₂ particles, then the energy density required for SLM forming can be reduced, and the densification can finally be improved. Some crystalline TiB₂ formed a coherent relationship with the matrix, while some broken TiB₂ particles did not, however, MgZn₂ and Al₃(Sc,Zr) can perform as intermediate phases to connect these non-coherent surfaces to aluminum matrix. All these factors lead to an increase in strength of the composite. The SLM-fabricated micron-sized TiB₂/AlZnMgCu(Sc,Zr) composite finally shows a very high ultimate tensile strength of ~646 MPa and yield strength of ~623 MPa, which are higher than many other aluminum composites fabricated by SLM, while maintaining a relatively good ductility of ~4.5%. The fracture of TiB₂/AlZnMgCu(Sc,Zr) composite is occurred along the TiB₂ particles and the bottom of the molten pool. This is due to the concentration of stress from the sharp tip of TiB₂ particles and the coarse precipitated phase at the bottom of the molten pool. The results show that TiB₂ plays a positive role in AlZnMgCu alloys fabricated by SLM, but finer TiB₂ particles should be studied.

Keywords: selective laser melting; TiB₂/AlZnMgCu(Sc,Zr) composites; heterostructure; Al₃(Sc,Zr); fracture behavior



Citation: Yin, P.; Liu, Y.; Liang, Z.; Pan, W.; Shao, S.; Zhang, Y. Microstructure, Mechanical Properties and Fracture Behavior of Micron-Sized TiB₂/AlZnMgCu(Sc,Zr) Composites Fabricated by Selective Laser Melting. *Materials* **2023**, *16*, 2112. <https://doi.org/10.3390/ma16052112>

Academic Editor: Alexander Yu Churyumov

Received: 8 February 2023
Revised: 28 February 2023
Accepted: 28 February 2023
Published: 6 March 2023



Copyright: © 2023 by the authors. Licensee MDPI, Basel, Switzerland. This article is an open access article distributed under the terms and conditions of the Creative Commons Attribution (CC BY) license (<https://creativecommons.org/licenses/by/4.0/>).

1. Introduction

In recent years, modern advanced industrial equipment, such as aviation, aerospace, electric power, petrochemical, shipbuilding and so on, is developing towards the direction of complex structure and high performance [1,2]. The requirements for manufacturing technology are increasingly high and the challenges are increasingly severe [3,4]. Selective laser melting (SLM) is a technology that uses a high-power laser to directly melt metal powder into a two-dimensional plane, then superpose layer by layer to form three-dimensional parts [5–8]. Compared with the traditional process, SLM can directly fabricate nearly fully dense complex parts, which has advantages in shortening production cycle and reducing cost, so it is widely used in military, aviation and aerospace fields [9–11].

Al-Zn-Mg-Cu alloys have been widely used in aerospace and automobile industry because of their excellent mechanical properties, extremely high strength-to-weight ratio, excellent thermal working performance, good corrosion resistance and other advantages [12,13]. Studies have shown that Al-Zn-Mg-Cu can form smaller and finer brittle S-phase (Al₂CuMg) precipitate at a cooling rate of more than 500 °C/h, thus obtaining better aging hardening effect during

subsequent heat treatment [14]. The extremely high cooling rate ($10^3\sim 10^6$ K/s) [15] of SLM has great potential for fabricating Al-Zn-Mg-Cu alloys.

However, Al-Zn-Mg-Cu alloys are difficult to weld for complex composition and large solidification temperature range. At the beginning of solidification process, the primary equilibrium phase solidifies preferentially, which leads to the enrichment of solute in the liquid near the solidification interface. Therefore, the temperature of local equilibrium liquid phase changes, resulting in local unstable supercooling state. The primary equilibrium then grows rapidly into columnar grain along the heat flow, leaving behind a thin layer of fluid between branches; after that, the fluid solidifies and shrinks to form cracks parallel to the columnar grain. In contrast, equiaxed grain adapt more easily to the thermal shrinkage strain associated with solidification [15]. Therefore, hot cracks can be effectively eliminated by increasing the proportion of equiaxed grains.

In order to eliminate the hot crack of Al-Zn-Mg-Cu alloys fabricated by SLM, many attempts have been made. John H. Martin et al. introduced Al_3Zr with basically complete coherent relation into aluminum matrix by adding ZrH_2 . In the process of SLM, Al_3Zr could be used as heterogeneous nucleation point to increase the proportion of equiaxed grain and refine the grains in the structure of SLM-formed alloy. Additionally, samples with excellent mechanical properties without cracks can be obtained. After heat treatment, the ultimate tensile strength (UTS) is close to 400 MPa and the fracture elongation (FE) is about 4% [15]. Li et al. alloyed Zr element and introduced Si element to increase melt viscosity and used low melting point silica-rich eutectic to fill cracks. In this paper, a new Si- and Zr-modified Al-Zn-Mg-Cu pre-alloying powder was developed for SLM, and the crack-free sample was successfully prepared. The synergistic effect of Si and Zr is helpful to obtain excellent tensile properties (UTS of about 446 MPa and FE of about 6.5% after being heat treated) [16]. Zhou et al. used TiB_2 instead of Zr to promote the nucleation of fine equiaxed grain. An Al-Zn-Mg-Cu powder co-incorporation with 4 wt.% Si and 2 wt.% TiB_2 was prepared by high energy ball milling. After addition of Si and TiB_2 , the formability of Al-Zn-Mg-Cu alloy was improved and the cracks were successfully eliminated, but there were a lot of pores. The UTS of Al-Zn-Mg-Cu sample formed by SLM was 556 MPa, and the fracture elongation (FE) was about 4.5% [17]. The presence of Si may generate harmful phase and reduce mechanical properties. For this reason, Zhu et al. introduced Sc with stronger grain refining effect rather than Si to eliminate thermal cracks. After composition design and process optimization, crack-free AlZnMgCu(Sc,Zr) alloy with unprecedented strength-ductility synergism was obtained by SLM. After heat treatment, the UTS was as high as 647 MPa and the FE was 11.6%, which was much higher than the strength of SLM-formed aluminum alloy reported so far [18].

In general, the main idea of eliminating hot cracks is to introduce a grain modifier in Al-Zn-Mg-Cu alloys, for example, adding melt modification elements such as Si, or introducing nucleating elements or ceramic particles to promote grain refinement. In the existing reports, it is generally achieved by pre-alloying powder preparation and externally addition of particle.

Pre-alloying powder is a method that modified elements or ceramic particles and the matrix composition were synchronously prepared into powder. Its advantage is that the modified elements or in situ reinforced particles could uniformly distribute in the powder. However, the process is complicated and the cost is high. In addition, the amount and shape of the added particles are not easy to control [19]. On the contrary, the method of adding particles externally is to mechanically mix the pre-alloyed matrix powder with the added powder (elemental powder or reinforced particles), then conduct SLM forming. This method can more easily adjust the composition and amount of added material, and effectively reduce the costs [20].

In various alloying elements, Sc and Zr elements have the best effect on eliminating thermal cracks during SLM forming process, because primary $Al_3(Sc,Zr)$ generated at high cooling rates can significantly increase the proportion of equiaxed grain and refine the grains. Study have shown that the thermal cracks can be completely eliminated when the

content of Sc and Zr reaches 0.6% and 0.36%, respectively [21], and its grain refinement effect can also make material both strong and tough. However, it is not economical to further increase the content of Sc and Zr elements to improve the strength due to the high price. Therefore, it is an option to use external ceramic particles to further enhance the strength by improving the laser absorption rate of powder, reducing splatter and refining the grain [19,22–25]. Besides, due to the high strength and modulus of ceramic particles, its addition can significantly improve the mechanical properties of alloys. However, it is also necessary to consider the binding between ceramic particles and matrix. Cracks may generate at interface between ceramics and matrix because of poorly matched thermal expansion coefficient and some brittle phase at the interface produced by harmful reactions [26,27]. On the contrary, stable and uniform interface reactions can improve mechanical properties [28]. Based on this consideration, TiB₂ has become an excellent enhancement in AlZnMgCu alloys for its advantages of high melting point, high strength, large modulus, less harmful reaction but good wettability and strong interface bonding with aluminum alloy and so on [29–33].

Therefore, in this paper, an AlZnMgCu(Sc,Zr) powder, which can be used for SLM forming crack-free samples, was prepared by pre-alloying method, and micron-sized TiB₂ was added by externally added particle method to further enhance the mechanical properties of the alloy. The effect of micron-sized TiB₂ on the microstructure and properties of AlZnMgCu(Sc,Zr) alloy was explored, and the mechanism was analyzed. This work would lay the foundation for obtaining lower cost and better performance of SLM formed high strength aluminum composites.

2. Materials and Methods

2.1. Powder Preparation

An AlZnMgCu(Sc,Zr) alloy powder prepared by inert gas atomized was used as the matrix of the composite powder, and its chemical composition was detected by inductively coupled plasma atomic emission spectroscopy (ICP-AES) (Table 1). As can be seen from Table 1, Zn, Sc, Zr and other elements were burned to a certain extent in the process of melting and gas atomization. Micron-sized TiB₂ particles (1–3 μm, 99%) purchased from Xuzhou Jiechuang New Material Technology Co. Ltd. were mixed into AlZnMgCu(Sc,Zr) alloy powder at 3 wt.%. The ball-to-powder weight ratio was 1.2:1, and the powder was mixed in a mixer for 15 h.

Table 1. The composition of AlZnMgCu(Sc,Zr) powder.

Elements/wt.%	Zn	Mg	Cu	Sc	Zr	Al
Design content	8.5	3	1	0.8	0.6	Bal.
Powder content	8.28	2.96	1.02	0.66	0.39	Bal.

A laser particle size analyzer (BT-9300S, Bettersize Instruments Ltd, Dandong, China) was used to test the particle size of the prepared composite powder. As the results showed in Supplementary Figure S1, the particle size of the TiB₂/AlZnMgCu(Sc,Zr) powder is in the range of 15 μm to 53 μm, with the D10, D50 and D90 of 14.73 μm, 27.37 μm and 43.91 μm, respectively, which met the particle size requirements for SLM forming.

The surface morphology of the TiB₂/AlZnMgCu(Sc,Zr) powder was observed by SEM, and the obtained image is shown in Figure 1. According to Figure 1a, the prepared composite powder has good sphericity. In Figure 1b, it is found that most of the fusiform TiB₂ particles adhered to the surface of the powder, and a small part scattered between the powder. The long diameter of TiB₂ particles is about 2–6 μm and the short diameter is about 1 μm.

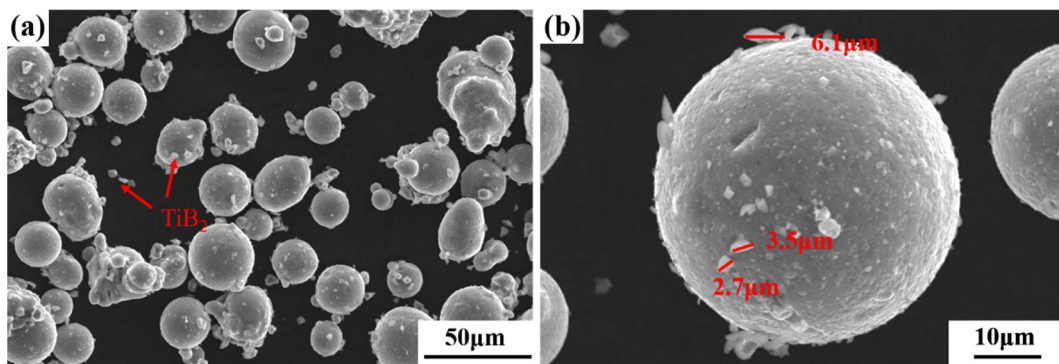


Figure 1. SEM morphology of 3 wt.% micron-sized $\text{TiB}_2/\text{AlZnMgCu}(\text{Sc,Zr})$ composite powder (a) in relatively low magnification and (b) in relatively high magnification.

2.2. Forming Process

In this experiment, the EP-M250 metal 3D printing system (Beijing Eplus3D Technology Co., Ltd., Beijing, China) was used to form samples, and the laser has a spot diameter of $70\ \mu\text{m}$ and a maximum power of 500 W. The oxygen content in the chamber of 3D printing system is strictly controlled below 100 ppm by filling with Ar gas and the temperature of substrate was preheated and maintained at $140\ ^\circ\text{C}$ before and during SLM processing. Keep hatch spacing (H) and the layer thickness (D) as constant, while laser power (P) and scanning speed (V) were adjusted to explore their major impact on the quality of the fabricated sample. The SLM process parameters was set as follows: $P = 230\sim 260\ \text{W}$, $V = 600\sim 1000\ \text{mm/s}$, $H = 0.1\ \text{mm}$, $D = 0.03\ \text{mm}$ and a parallel scanning strategy whose scanning direction rotating is 67° per layer was selected.

Horizontal samples whose size is $60\ \text{mm} \times 10\ \text{mm} \times 11\ \text{mm}$ was printed for subsequent exploration, as shown in Supplementary Figure S2. The long axis of horizontal samples was perpendicular to the building direction (BD), as demonstrated in Figure 2. After several rounds of preliminary process screening, the optimum forming process (OFP) for micron-sized $\text{TiB}_2/\text{AlZnMgCu}(\text{Sc,Zr})$ composite was $P = 230\ \text{W}$, $V = 800\ \text{mm/s}$ (A3 sample in Supplementary Figure S2). Moreover, its energy density (E) was $95\ \text{J/mm}^3$, calculated by Formula (1) [23]:

$$E = P / (V \times H \times D) \quad (1)$$

The forming process of matrix powder $\text{AlZnMgCu}(\text{Sc,Zr})$ alloy have also been studied, where the optimum forming process is $P = 250\ \text{W}$, $V = 760\ \text{mm/s}$ and $E = 110\ \text{J/mm}^3$. This part of the work will be described in another article. Compared with $\text{AlZnMgCu}(\text{Sc,Zr})$ alloy, the optimum forming energy density decrease after the addition of micron-sized TiB_2 .

The chemical composition of composite powder and formed sample are shown in Table 2. A large amount of Zn element and a small amount of Mg element are vaporized and blown away in the form of soot during the forming process, resulting in the reduction of Zn and Mg content in the fabricated sample. The sum of Ti element and B element in the formed sample is about 3 wt.%, indicating that the micron-sized $\text{TiB}_2/\text{AlZnMgCu}(\text{Sc,Zr})$ composite has been successfully prepared. The theoretical density of the formed sample is $2.841\ \text{g/cm}^3$.

Table 2. The composition of micron-sized $\text{TiB}_2/\text{AlZnMgCu}(\text{Sc,Zr})$ powder and the formed sample.

Elements/wt.%	Zn	Mg	Cu	Ti	B	Sc	Zr	Al
Powder	8.44	3.12	0.98	1.34	0.52	0.66	0.40	Bal.
Sample	6.24	2.60	1.01	2.05	0.85	0.68	0.41	Bal.

2.3. Experimental Procedures

The density of the composite sample was measured by direct reading solid densitometer (SJ-300G, Shanghai Shuju Instrument Technology Co., Ltd., Shanghai, China), whose

working principle is Archimedes drainage method, the ratio of the measured value to the theoretical density was calculated as the densification of the fabricated sample. The horizontal samples were cut into small specimen of 10 mm × 10 mm × 10 mm along the building direction, then the surfaces of the specimen were ground with waterproof abrasive paper and polished to mirror surface by polishing cloth. Internal defects and particle distribution were observed by Axiovert 200 MAT optical microscope (OM). X-ray Computed Tomography (CT), Volume 1 x s 240/180, GE Sensing & Inspection Technologies GmbH, Frankfurt, Germany, was performed to highlight the defects within the entire volume of the sample. The following settings were used for the measurements: (i) voltage of 110 kV; (ii) 6.228 μm as resolution of the detector; (iii) 120 min as scanning time. JSM-7900F field emission scanning electron microscope (SEM) equipped with electronic channel contrast (ECC) and electron backscatter diffraction (EBSD, scanning step 0.05 μm) were used to observe and analyze the microstructure of grains. X'Pert Pro MPd polygrainline X-ray diffraction analyzer (XRD) from the Netherlands was used to determine the phase composition of the samples. The working tube voltage was 40 kV, the working current was 40 mA and the scanning step was 0.033°. The microstructures of the interfaces and precipitates were investigated by FEI Tecnai F20 transmission electron microscope (TEM, acceleration voltage 200 kV) equipped with an energy-dispersive X-ray spectrometer (EDX) and a high-angle annular dark field (HAADF).

The TiB₂/AlZnMgCu(Sc,Zr) composite specimens fabricated by SLM were heat treated with solution treatment at 470 °C for 1 h and then aged at 120 °C for 24 h after quenching in water. The as-printed and heat-treated samples were processed into tensile bar, as shown in Supplementary Figure S3 for mechanical property test, and the room temperature tensile test was carried out by the Quasar10 tensile testing machine. The test standard was GB/T 228.1-2010. Each result was validated at least three times. The samples were cut into tensile pieces along the vertical and horizontal planes respectively to observe the microstructure on the side of the fracture surface after tensile fracture, as shown in Figure 2.

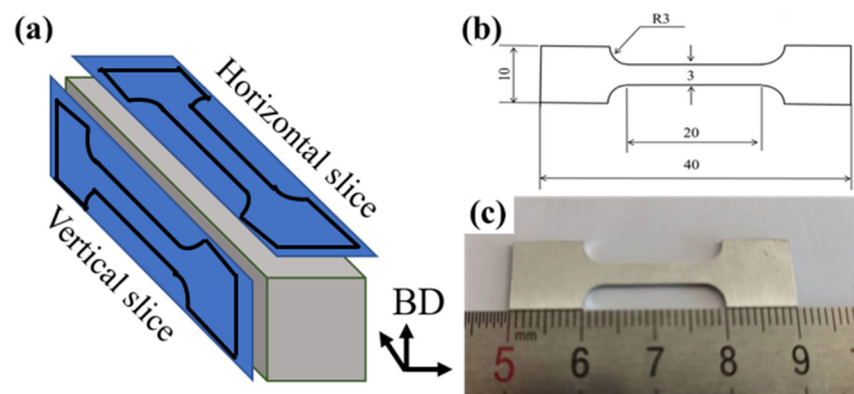


Figure 2. Diagram of tensile plate (a) horizontal sample, building direction (BD) and sampling direction, (b) schematic diagram (mm) and (c) real sample.

3. Results and Discussion

3.1. Defects and Microstructures Analysis

The microstructure image of the fabricated sample before and after the addition of TiB₂ is shown in Figure 3. As shown in Figure 3a,b, there are no cracks in the AlZnMgCu(Sc,Zr) alloy samples obtained by the optimal SLM forming process, but a large number of pores exist, shown as black dots and indicated by the red arrows in the figure. The microstructure of the TiB₂/AlZnMgCu(Sc,Zr) composite sample is shown in Figure 3c,d. It can be seen from the figure that there are no cracks in the composite material, with only a few pores inside, as shown by the red arrows. The average size of pores in TiB₂/AlZnMgCu(Sc,Zr) composite sample is about 8 μm, and Supplementary Figure S4 shows the size distribution of pores. The

porosity of $\text{TiB}_2/\text{AlZnMgCu}(\text{Sc,Zr})$ composite samples is less than that of $\text{AlZnMgCu}(\text{Sc,Zr})$ alloy samples, which is also consistent with the increase of densification. Moreover, the light gray spindle-shaped dot phases indicated by the blue arrows in the image are the micron-sized TiB_2 particles. In the composite material, TiB_2 particles are uniformly distributed in the matrix, with no obvious agglomeration. Besides, TiB_2 particles are well combined with the matrix, and no cracks or inclusions were found around the particles.

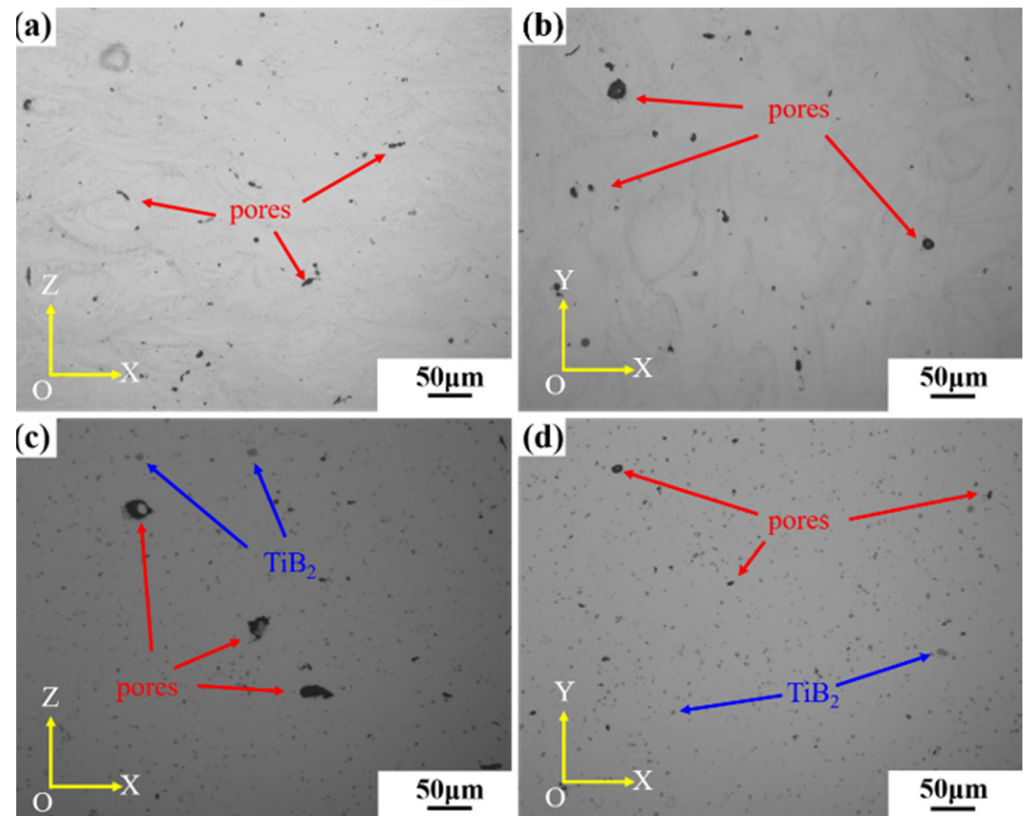


Figure 3. Metallography of SLM formed as-printed specimen: (a) vertical plane of $\text{AlZnMgCu}(\text{Sc,Zr})$ alloy, (b) horizontal plane of $\text{AlZnMgCu}(\text{Sc,Zr})$ alloy, (c) horizontal plane of $\text{TiB}_2/\text{AlZnMgCu}(\text{Sc,Zr})$ composite and (d) horizontal plane of $\text{TiB}_2/\text{AlZnMgCu}(\text{Sc,Zr})$ composite.

The densification of the composites is 99.67%, tested by electronic solid densitometer. Compared with the 98.7% densification of $\text{AlZnMgCu}(\text{Sc,Zr})$ sample fabricated by the optimal SLM process in the previous experiment, samples with higher density can be obtained by the addition of micron-sized TiB_2 by improving the laser absorption rate of powder [17,19,22]. The pore volume of composite samples was measured by industrial CT, and the defect volume ratio is 0.24%, which means that the density of the sample is 99.76%, which is consistent with the density measured by the electronic solid densitometer. The distribution of defects inside the sample is shown in Supplementary Figure S5. Most of the pores in the samples were spherical, which is consistent with the characteristics of volatile pore. There is also a small number of irregular pores, which is believed to be gaps of some incomplete melting powder. All these pores are uniformly distributed in the matrix. The size and shape of pores have great influence on Young's modulus, UTS and fracture behavior. There are more concentration points around large pores and irregular pores, where cracks are more likely to start and propagate nearby. The rounder the shape of the pore, the more uniform the stress distribution nearby, and the higher the Young's modulus and UTS of the material [34]. The surface morphology of the formed sample was observed by using SEM, and EDS scanning was performed for the distribution of the elements. The results are shown in Figure 4, where the bright white fusiform particles in

Figure 4a are TiB_2 particles with irregular shape and some sharp tips, whose particle size is about 5 μm . The general shape of the molten pool can be observed in Figure 4a.

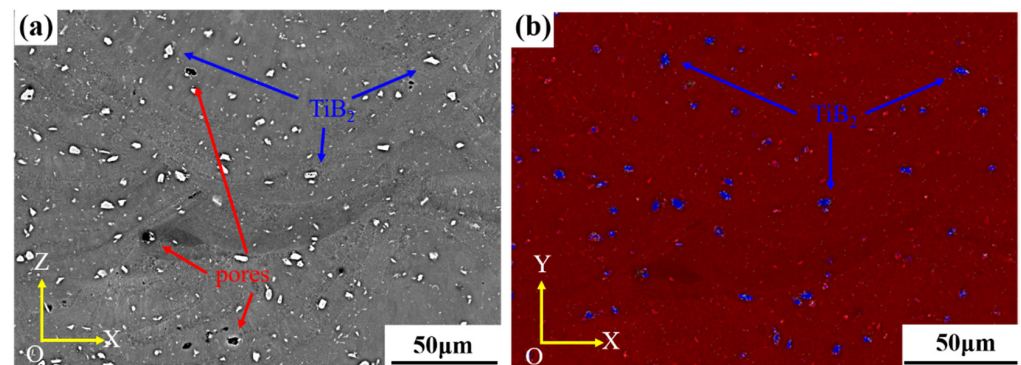


Figure 4. The microstructure of as-printed $TiB_2/AlZnMgCu(Sc,Zr)$ composite samples: (a) SEM and (b) EDS planar scanning.

The microstructure of the $TiB_2/AlZnMgCu(Sc,Zr)$ composite sample after heat treatment is shown in Figure 5. TiB_2 particles are randomly distributed in the equiaxed fine grain (FG) region and columnar grain (CG) region. The shape and size of TiB_2 particles are almost unchanged. In addition, there are equiaxed bright white particles distributed in the matrix. Unlike TiB_2 particles, these equiaxed bright white particles are more concentrated in the equiaxed fine grain region, which are speculated to be precipitated phase after heat treatment.

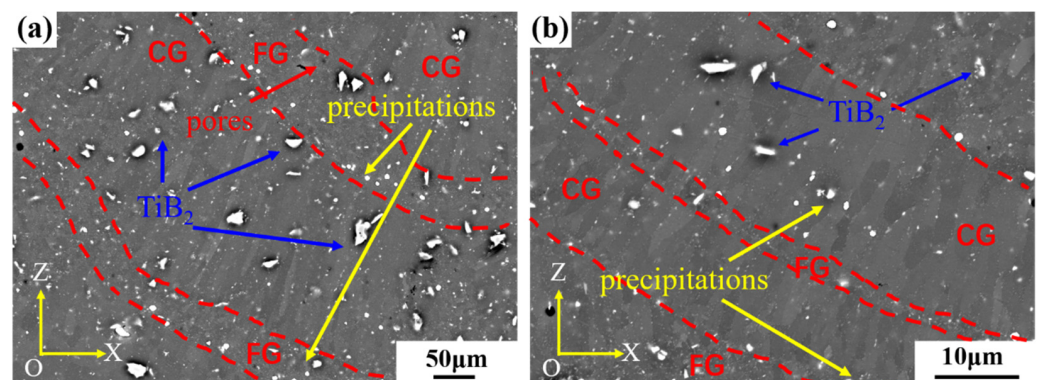


Figure 5. The microstructure of heat-treated $TiB_2/AlZnMgCu(Sc,Zr)$ composite samples (a) in relatively low magnification and (b) in relatively high magnification.

Figure 6 shows the EBSD inverse polar diagram and grain size distribution of the vertical section of $AlZnMgCu(Sc,Zr)$ alloy sample formed by SLM. It can be seen from the figure that the aluminum alloy has a typical heterostructure with columnar grain and equiaxed fine grain alternately arranged, which make $AlZnMgCu(Sc,Zr)$ alloy samples fabricated by SLM both strong and tough [35,36]. Compared with Figure 6a,b and Figure 6c,d, the grain size does not decrease but rather increases after the addition of micron-sized TiB_2 . The grain size of equiaxed grain is about 1 μm and the columnar grain is about 5 μm in $AlZnMgCu(Sc,Zr)$ alloy, while the equiaxed grain is about 1.5 μm and the columnar grain is about 9 μm in $TiB_2/AlZnMgCu(Sc,Zr)$ composite. As we can see by comparing Figure 6e,f and Figure 6c,d, after heat treatment, the grain size of $TiB_2/AlZnMgCu(Sc,Zr)$ composite is further coarsened. The grain size of equiaxed grain increases to about 1.5 μm and the grain size of columnar grain also increases a little.

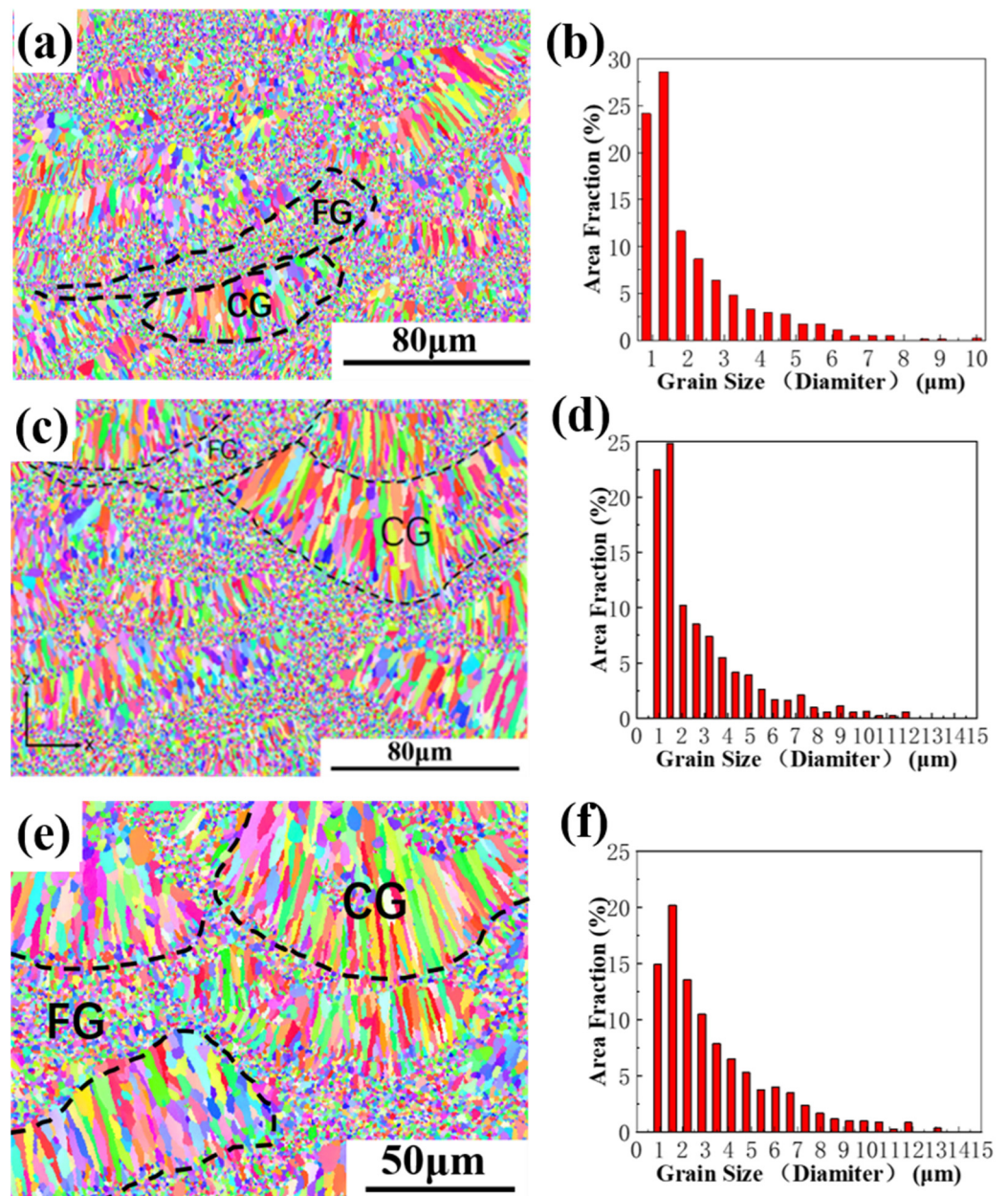


Figure 6. EBSD analysis and grain size distribution in vertical plane of SLM forming specimen (a,b) as-printed AlZnMgCu(Sc,Zr) alloy, (c,d) as-printed TiB₂/AlZnMgCu(Sc,Zr) composite and (e,f) heat-treated TiB₂/AlZnMgCu(Sc,Zr) composite.

3.2. Precipitated Phase and Interface Analysis

TEM analysis was used to further observe the microstructure of the as-printed composites. Figure 7a,b show the microscopic morphology of the boundary between equiaxed grain and columnar grain in a single molten pool. Comparing the bright field image with the high-angle annular dark field (HAADF) image, it is found that the strip precipitates are evenly distributed along the grain boundaries, and there are some nano-sized round particles in the equiaxed grain boundaries and columnar grain. In addition, the intact micron-sized TiB₂ particles are embedded between columnar grains. The diameter of equiaxed grain is 0.5~1 μm and the length of columnar grain is about 6~10 μm.

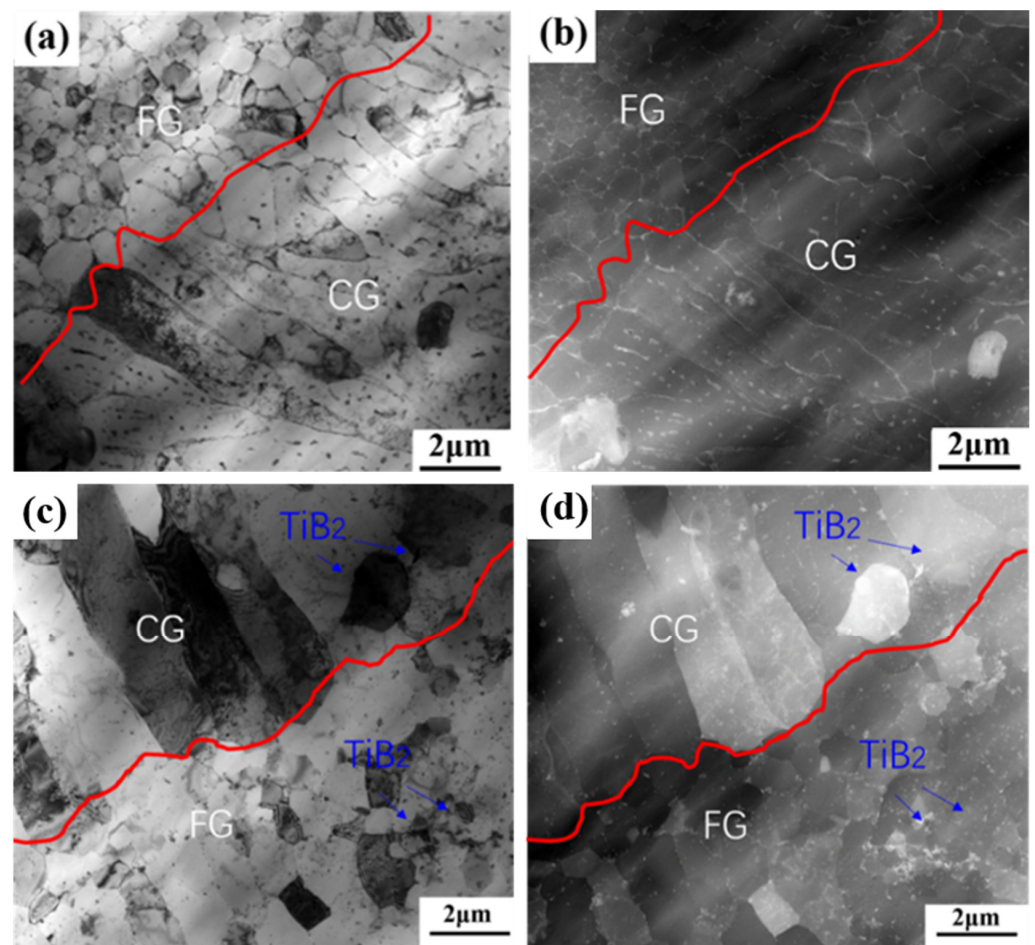


Figure 7. Morphological characteristics of equiaxed and columnar grain in $\text{TiB}_2/\text{AlZnMgCu}(\text{Sc,Zr})$ composite under STEM, as-printed state: (a) bright filed (b) HAADF and heat-treated state: (c) bright filed and (d) HAADF.

After heat treatment, there are some changes on the microstructure of $\text{TiB}_2/\text{AlZnMgCu}(\text{Sc,Zr})$ composite, shown in Figure 7c,d. The most obvious change is that there is no banded precipitate at the grain boundary, which becomes clean. The amount of nano-sized round precipitated particles decrease in the columnar grain region, while increase in the equiaxed grain region. In addition, the equiaxed grains only have limited growth, the average diameter is about 1.3 μm and the columnar grains have coarsened a little.

There are some changes in the precipitated phase after heat treatment observed in STEM, as shown in Figure 7. However, these changes are hard to identify in phase diagrams, as depicted in Supplementary Figure S5. The reason for this may be the small grain size and low volume fraction of the precipitates, which makes forming discernible peaks in the phase diagram difficult. In order to clarify the phase composition of the precipitated phase, EDS scanning was performed in the equiaxed grain region and the columnar grain region, and the results are shown in Figure 8. In Al matrix, a small amount of Mg and Zn elements are solidly dissolved, and a large amount of Mg and Zn elements are uniformly enriched at the grain boundaries of the equiaxed fine grain region and columnar grain region. Due to the higher energy at the grain boundary, continuous precipitations are formed along the grain boundaries by homogeneous enrichment of Mg and Zn elements [16,18]. In addition, the Mg and Zn elements can be precipitated into a granular MgZn_2 precipitated phase due to the partial remelting and thermal effects of SLM laser scanning in the later layer. The grains in the equiaxed grain region are generally only subjected to the thermal history of

melting and rapid solidification by laser heating, so there is almost no MgZn_2 precipitated phase within the grains.

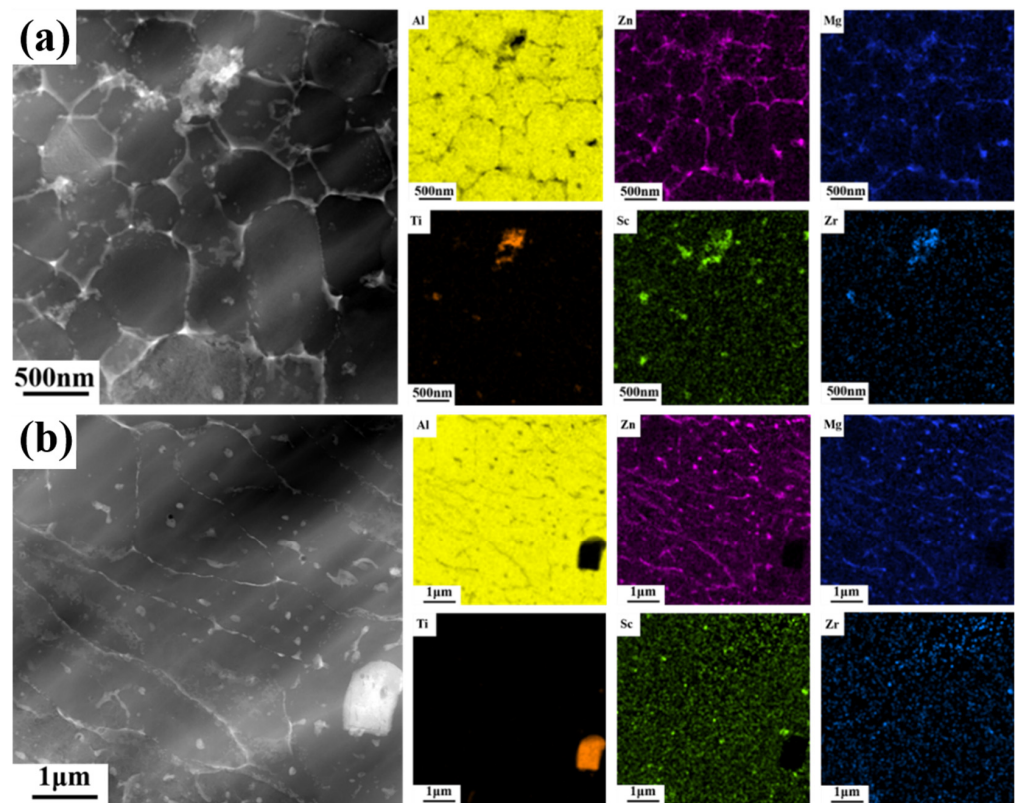


Figure 8. STEM HAADF images of SLM-fabricated $\text{TiB}_2/\text{AlZnMgCu}(\text{Sc,Zr})$ composite as-printed samples and corresponding EDX mapping of the solute elements (Al, Zn, Mg, Ti, Sc, Zr) (a) in the fine grain region and (b) in the columnar grain region.

Sc and Zr elements are slightly different. Regardless of equiaxed grain zone or columnar grain, Sc and Zr elements do not accumulate along grain boundaries, and most of them are solidly dissolved in Al matrix, while a small amount is precipitated into nano-sized $\text{Al}_3(\text{Sc,Zr})$ particles within grain boundaries. The reasons for this could be as follows: when the bottom of the molten pool contacts with the solidified previous layer, it will cause a very high cooling rate and temperature gradient, which is conducive to the precipitation of primary $\text{Al}_3(\text{Sc,Zr})$, and these primary $\text{Al}_3(\text{Sc,Zr})$ can act as the nucleation center to form ultra-fine grain [37,38]. Columnar grains are grown from the outer edge of equiaxed grains, and may be introduced some primary $\text{Al}_3(\text{Sc,Zr})$ [21]. More likely, a small amount of secondary $\text{Al}_3(\text{Sc,Zr})$ is precipitated similar to Mg and Zn elements.

In addition, by observing the distribution of elements near TiB_2 , it can be found that there is enrichment of Mg, Zn, Sc and Zr elements around some broken TiB_2 particles in Figure 8a. However, this phenomenon does not exist around the intact large particle TiB_2 in Figure 8b. The reason for this is that the intact particle TiB_2 has a good interfacial combination with the aluminum matrix, while the broken TiB_2 particle has a high free energy similar to the grain boundary, in which is easy to dissolve Mg, Zn, Sc and Zr elements. In addition, the atomic arrangement on the surface of broken TiB_2 particles is complex and the interface between those surfaces and aluminum matrix is poor. A small amount of precipitated Mg ($\text{Zn}_{1.5}\text{Cu}_{0.5}$) phase can be used as the interphase to improve the overall interface bonding [32,33].

After heat treatment, the distribution of elements changes significantly, as shown in Figure 9. The continuous precipitation at grain boundary disappeared after heat treatment, and the grain boundary became clean and smooth. Mg, Zn and Cu element were uniformly

distributed, with only a small number of granular precipitates. In the solution treatment stage, Mg, Zn and Cu element redissolved, while in the aging stage, Mg, Zn and Cu element precipitated in the form of particles at the grain boundary, because of the high energy density of the grain boundary. The number of precipitated particles in the fine grain region was also more than that in the columnar grain region, because there were more grain boundaries in the fine grain region.

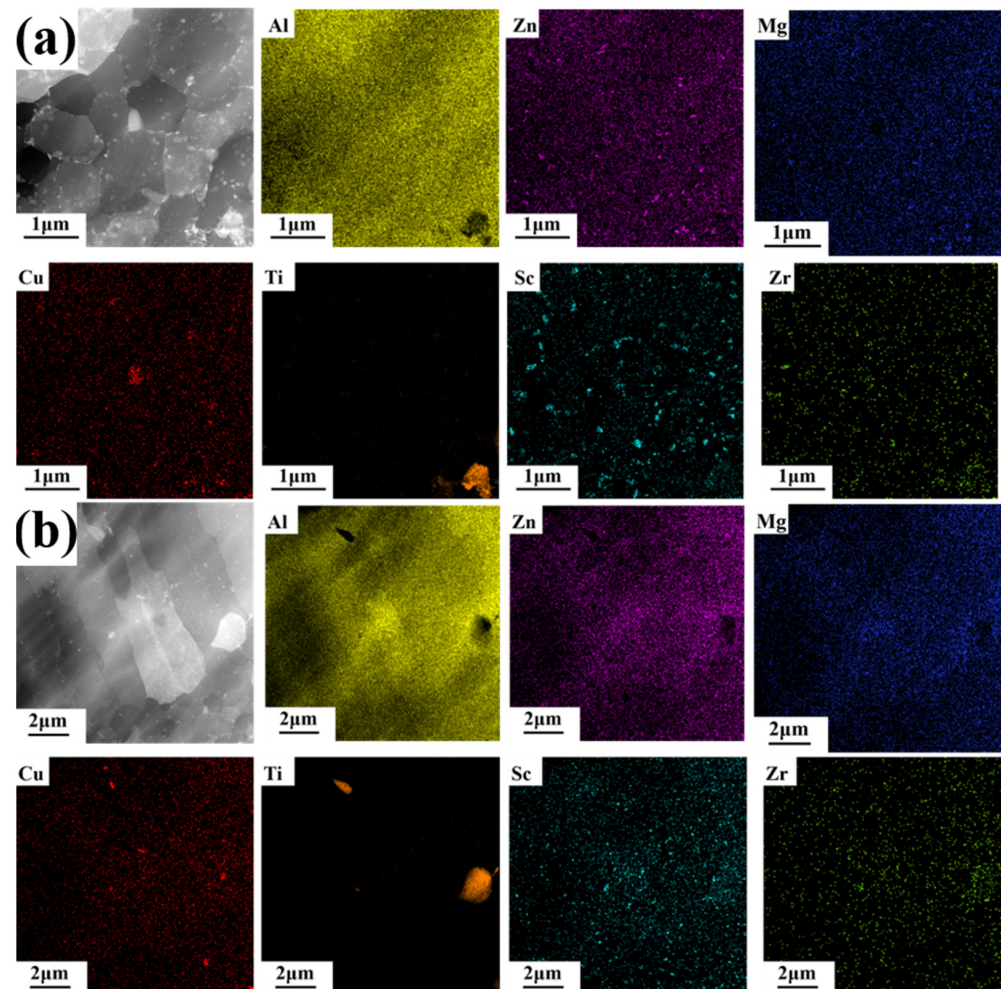


Figure 9. STEM HAADF images of SLM-fabricated $\text{TiB}_2/\text{AlZnMgCu}(\text{Sc,Zr})$ composite heat-treated samples and corresponding EDX mapping of the solute elements (Al, Zn, Mg, Cu, Ti, Sc, Zr) (a) in the fine grain region and (b) in the columnar grain region.

Due to the non-equilibrium solidification process caused by extremely high cooling rate in SLM forming process, a large number of Sc and Zr elements were oversaturated in the matrix, then during the heat treatment, these Sc and Zr element elements in oversaturated solid solutions will be precipitated into secondary $\text{Al}_3(\text{Sc,Zr})$ [39,40]. Besides, due to the faster solidification, the amount of Sc and Zr elements in solid solution at the bottom of the molten pool is also higher; moreover, there are more grain boundaries in the fine grain area, which can provide rapid diffusion channels. Therefore, there are more and coarser precipitated particles at the bottom of the molten pool than in the columnar grain region.

Figure 10 presents the interface between micron-sized TiB_2 particle and Al matrix in SLM-fabricated $\text{TiB}_2/\text{AlZnMgCu}(\text{Sc,Zr})$ composite; it can be seen that there is a transition layer of about 5 nm between TiB_2 particles and Al matrix, and the atoms of the transition layer are misaligned. After calibration of the diffraction pattern from the interface, it is found that there are two orientation relations. They are OR1: $(0001) [11-20]\text{TiB}_2 // (-111) [110]\text{Al}$

and OR2: $(-110-1) [11-20]TiB_2 // (002) [110]Al$, respectively, as also reported by [19,32,41], indicating that the interface between TiB_2 particles and Al matrix are well combined.

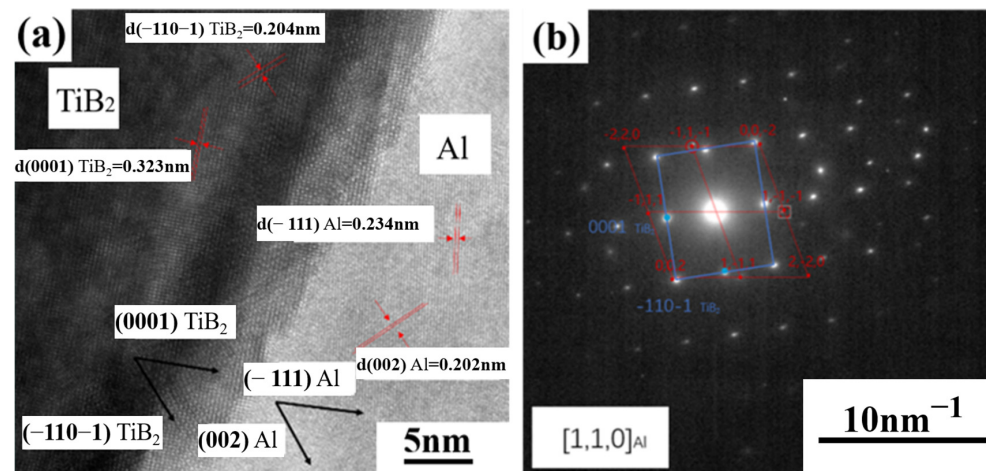


Figure 10. (a) HRSTEM image of the interface between micron- TiB_2 particle and Al matrix in SLM-fabricated $TiB_2 / AlZnMgCu(Sc,Zr)$ composite and (b) indexing of the SAED patterns, showing relative orientation relations (ORs).

Crystal structure models of interface between TiB_2 and aluminum matrix are established to further analyze the interface binding, as shown in Figure 11. The edge-to-edge matching (E2EM) crystallography model is used to calculate the atomic spacing mismatch (F), and the calculation Formula (2) [42] is as follows:

$$F = |D_m - D_p| / D_p \quad (2)$$

where D_m and D_p represent the interatomic distances between the metal matrix and ceramic particles in the close-packed or nearly close-packed directions, respectively.

Figure 11a represents the crystal plane of $(-111)Al$ and $(0001)TiB_2$, which have the same structure and similar lattice spacing. The atomic spacing mismatch of the most close-packed and nearly close-packed directions are calculated to be 6.2% and 9.8%, respectively, showing a good coherent relationship. $Al_3(Sc,Zr)$ has the same grain structure as aluminum matrix, but the lattice spacing is slightly larger. In the same crystal plane pair with TiB_2 , the atomic spacing mismatch of the most close-packed and nearly close-packed directions are calculated to be 4.4% and 4.5%, respectively, showing an excellent coherent relationship, as represented in Figure 11b. Therefore, $Al_3(Sc,Zr)$ has a better interface binding with TiB_2 than aluminum matrix dose, so it is more likely to cause enrichment of Sc and Zr elements around TiB_2 .

This phenomenon indicates that TiB_2 and Sc, Zr element interact with each other and act synergistically in Al matrix composites. On the one hand, it is beneficial to the interface bonding between the reinforcement phase and the matrix, and enhance the strength of the composite material. On the other hand, the evenly distributed precipitation phase $Al_3(Sc,Zr)$ will be reduced, and the effect of precipitation strengthening will be weakened. These results indicate that there are new considerations in the composition design and strengthening mechanism of Sc, Zr micro-alloyed aluminum matrix composites reinforced with TiB_2 formed by SLM.

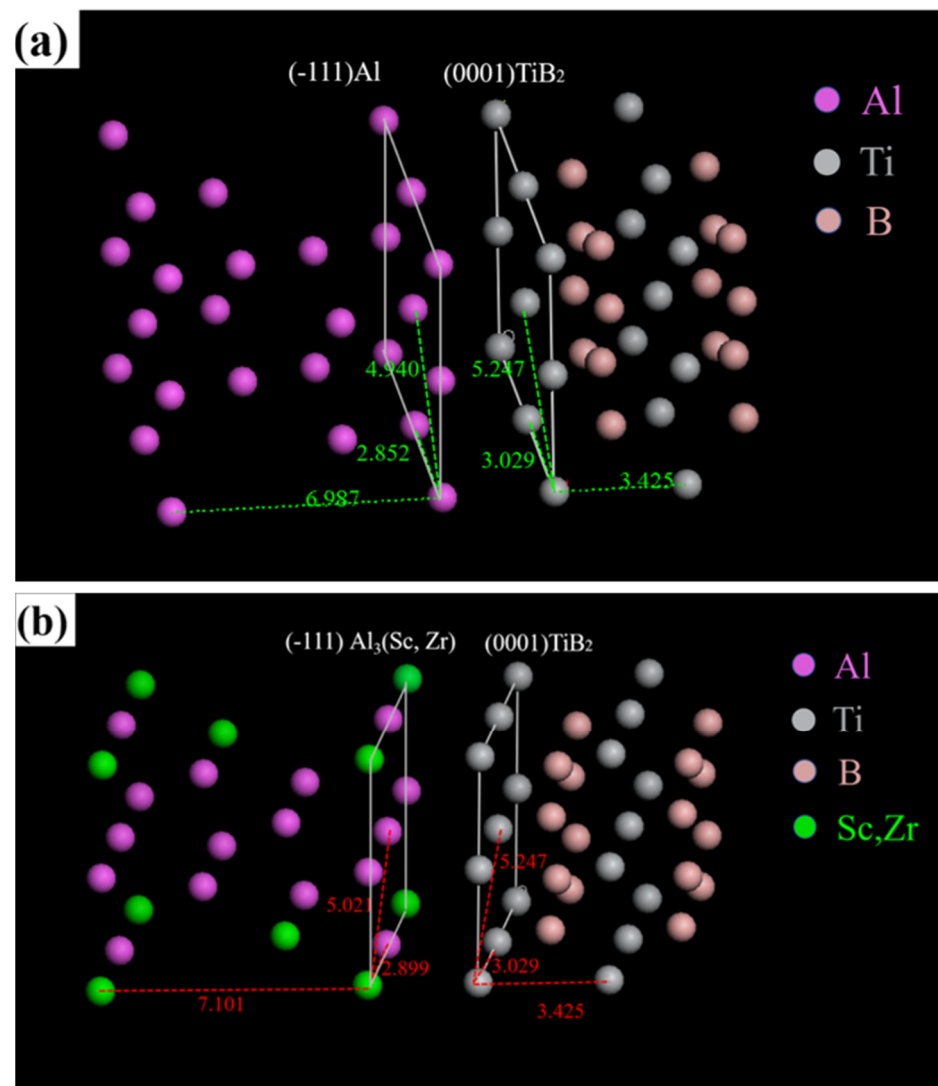


Figure 11. Crystal structure models of interface between TiB₂ and AlZnMgCu(Sc,Zr) matrix, (a) (−111)Al and (0001)TiB₂, (b) (−111)Al₃(Sc,Zr) and (0001)TiB₂.

3.3. Mechanical Properties

Table 3 shows that the mechanical properties of AlZnMgCu(Sc,Zr) alloys and micron-sized TiB₂/AlZnMgCu(Sc,Zr) composites after heat treatment with the same process have similar changes: after heat treatment, the tensile strength and yield strength of AlZnMgCu(Sc,Zr) alloys increase about 131 MPa and 155 MPa, respectively, and elongation decreases by about 10.7%. The tensile strength and yield strength of TiB₂/AlZnMgCu(Sc,Zr) composites increase about 136 MPa and 159 MPa, respectively, and elongation decreases by about 8.5%. The reason for this is that the heat treatment process is mainly regulated by precipitation of Al₃(Sc,Zr) and MgZn₂ phases, and the addition of micron-sized TiB₂ particles has little effect on the heat treatment process. However, the addition of micron-sized TiB₂ particles improve the mechanical properties. By comparing the mechanical properties of as-printed TiB₂/AlZnMgCu(Sc,Zr) composites and as-printed AlZnMgCu(Sc,Zr) alloys, the tensile strength has increased by about 7.5%, the yield strength has hardly increased, and the elongation after fracture has decreased by about 19.4%. The properties of heat-treated states are similar, where the tensile strength has increased by about 6.6%, the yield strength has increased by about 3% and the elongation after fracture has decreased by about 15.1%. The heat-treated TiB₂/AlZnMgCu(Sc,Zr) composite samples obtained by SLM have extremely high strength, where the ultimate tensile strength is about 646.7 MPa and the yield

strength is about 623 MPa. In addition, plasticity was preserved, as its elongation after fracture is about 4.5%. Its comprehensive mechanical properties exceed most of the SLM forming aluminum composites reported so far [17,19,20,41,43–47], as shown in Figure 12.

Table 3. Comparison of mechanical properties of AlZnMgCu(Sc,Zr) alloy and TiB₂/AlZnMgCu(Sc,Zr) composite before and after heat treatment.

Samples		UTS (MPa)	YS (MPa)	Elongation (%)
AlZnMgCu(Sc,Zr)	As-printed	475.3 ± 0.8	448.7 ± 4.0	16.0 ± 0.5
	Heat treated	606.7 ± 14.5	603.7 ± 18.0	5.3 ± 1.5
TiB ₂ /AlZnMgCu(Sc,Zr)	As-printed	510.8 ± 16.5	452.3 ± 17.1	13.0 ± 1.3
	Heat treated	646.7 ± 9.0	623.1 ± 22.6	4.5 ± 2.3

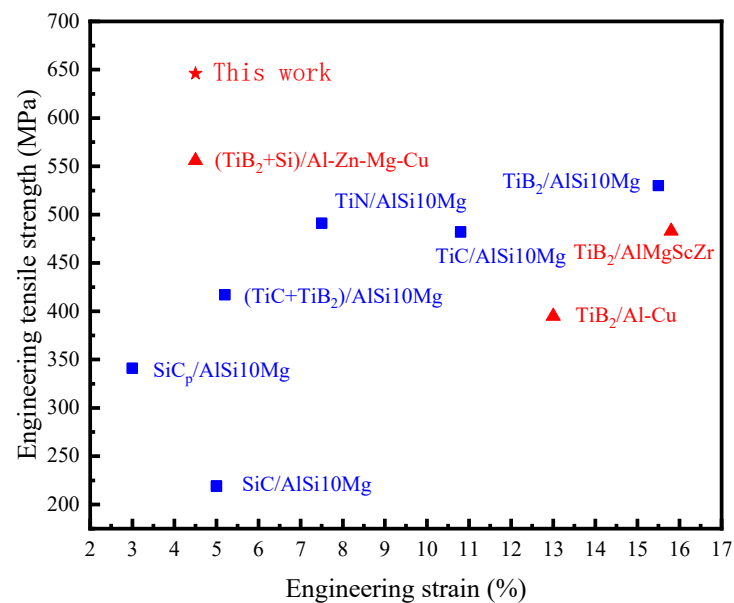


Figure 12. Comparison of mechanical properties of aluminum matrix composites formed by SLM [17,19,20,41,43–47].

3.4. Fracture Behavior

The fracture morphology of as-printed micron-sized TiB₂/AlZnMgCu(Sc,Zr) composite is shown in Figure 13. It is found that the fracture has a lot of honeycombs structure at low magnification, which is a typical plastic fracture. There are many defects on the surface of the fracture, which are mainly round pores, but no macroscopic cracks are found. Under high magnification electron microscopy, a large number of dimple structures could be observed, and there are some tiny precipitated phases at the bottom of the dimples. In addition, exposed TiB₂ particles separated from the matrix could be found. The fracture morphology shows that the fracture of micron-sized TiB₂/AlZnMgCu(Sc,Zr) composite formed by SLM occurs at pores, defects and the interface between the TiB₂ particles and Al matrix.

The tensile plates were sliced vertically and horizontally, and the microstructure of the side of the fracture were observed by SEM after being grinded and polished; the results are shown in Figure 14. Because the specimens being formed are horizontal, tensile direction (TD) is perpendicular to build-up direction (BD). As can be seen from Figure 14, the direction of growth of crack has little relationship with the shape of molten pool during fracture in as-printed TiB₂/AlZnMgCu(Sc,Zr) composite. After tensile deformation, the crack passes through the columnar and equiaxed grain regions completely. Moreover, there are TiB₂ particles and grooves left by debonding of TiB₂ particles near the fracture. The observation above indicates that the sharp tip of TiB₂ will cause concentration of stress, which leads to crack propagation.

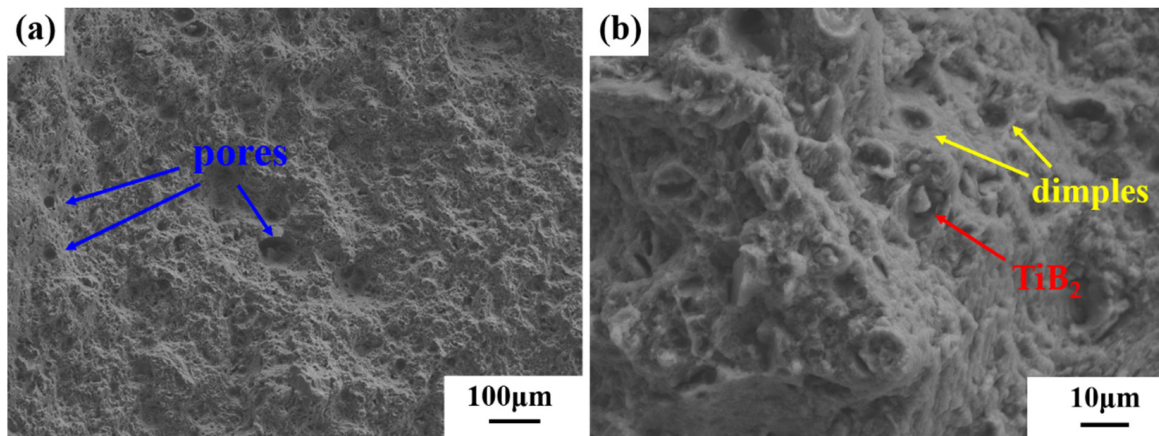


Figure 13. Fracture surfaces of SLM-fabricated $\text{TiB}_2/\text{AlZnMgCu(Sc,Zr)}$ composite as-printed sample (a) in relatively low magnification and (b) in relatively high magnification show dimples.

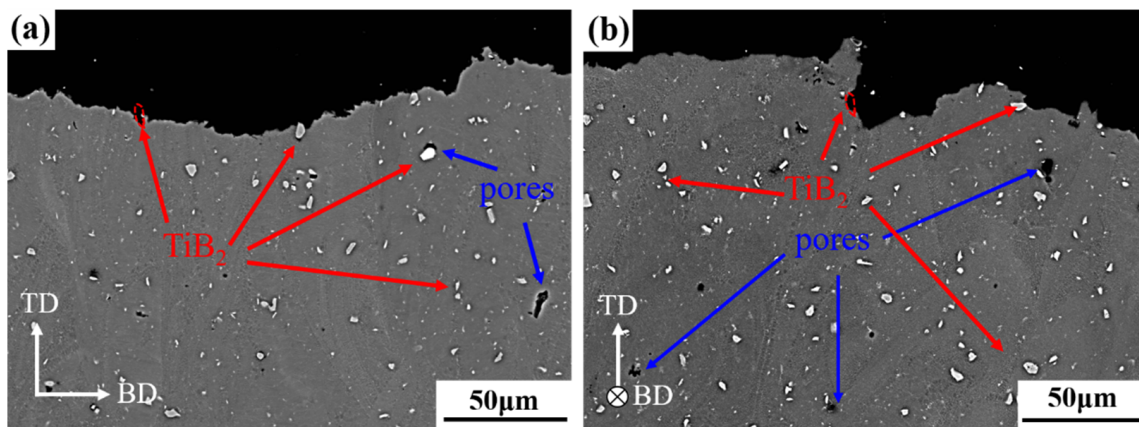


Figure 14. Fracture side surfaces of SLM-fabricated $\text{TiB}_2/\text{AlZnMgCu(Sc,Zr)}$ composite as-printed sample in relatively low magnification: (a) vertical plane and (b) horizontal plane.

Heat-treated $\text{TiB}_2/\text{AlZnMgCu(Sc,Zr)}$ composite samples were sliced along the vertical direction, and the comparison results with the as-printed state are shown in Figure 15. According to Figure 15b, TiB_2 particles and grooves left by TiB_2 particles after debonding also exist in the crack passing through the sample in heat treatment state. The difference is that the crack has a tendency to proceed along the equiaxial fine grain zone, which is the bottom of the molten pool. A possible reason for this is that the large precipitated phase at the bottom of the molten pool, as analyzed in Figure 9, may cause a concentration of stress, so it is easier for cracks to propagate in the fine grain zone [48]. Therefore, in the heat-treated $\text{TiB}_2/\text{AlZnMgCu(Sc,Zr)}$ composite specimens, the crack generally expands along the equiaxed grain zone and the interface between TiB_2 and the matrix.

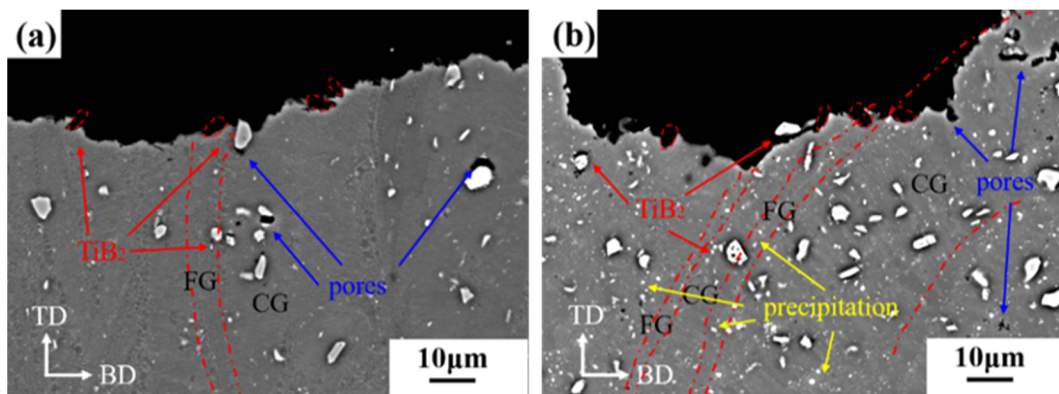


Figure 15. Fracture side surfaces of SLM-fabricated $\text{TiB}_2/\text{AlZnMgCu}(\text{Sc,Zr})$ composite vertical plane in relatively high magnification: (a) as-printed sample and (b) heat-treated sample.

4. Conclusions

In this paper, the micron-sized $\text{TiB}_2/\text{AlZnMgCu}(\text{Sc,Zr})$ composites fabricated by SLM are investigated. The differences of micron-sized $\text{TiB}_2/\text{AlZnMgCu}(\text{Sc,Zr})$ composite and $\text{AlZnMgCu}(\text{Sc,Zr})$ alloy samples in terms of macroscopic defects, microstructure, interface, mechanical properties and fracture behavior are compared between the as-printed and heat-treated samples. The main conclusions are as follows:

1. The crack-free micron-sized $\text{TiB}_2/\text{AlZnMgCu}(\text{Sc,Zr})$ composite with good surface quality and high densification of 99.76% have been successfully prepared by SLM. Micron-sized TiB_2 particles are distributed uniformly in the matrix. The addition of TiB_2 leads to an increase of densification, but has little influence on the microstructure, phase composition and heat-treatment process.
2. The complete micron-sized TiB_2 particle surface has a good interface with the aluminum matrix and the interface is clean and smooth, with no other intermediate phase. A large number of alloy-elements are enriched near the irregular surface of these broken TiB_2 , for relatively high surface free energy, similar to grain boundaries. Due to the poor interfacial bonding between these parts of the surface and the aluminum matrix, the $\text{Mg}(\text{Zn}_{1.5}\text{Cu}_{0.5})$ phase can form as the interphase to bond the matrix. The reason for this is that its lattice parameter at a specific crystal plane is between the TiB_2 and aluminum matrix.
3. The addition of micron-sized TiB_2 particles has a beneficial effect on the mechanical properties of $\text{AlZnMgCu}(\text{Sc,Zr})$ samples, and the increase is about 6%. The main reason for the increase is the increase of densification due to the increase of the powder laser absorption rate. In contrast, due to the introduction of brittle ceramic particles and its stress concentration effect, the ductility has decreases by about 15%. The ultimate tensile strength and yield strength of the composite are about 646 MPa and 623 MPa, respectively. Moreover, the composite has some plasticity and elongation after fracture, which is about 4.5%.
4. The fracture of the micron-sized $\text{TiB}_2/\text{AlZnMgCu}(\text{Sc,Zr})$ composite is due to the stress concentration of the sharp tips of TiB_2 . In addition, the large particles precipitated after heat treatment are mainly concentrated in the fine grain zone at the bottom of the molten pool, and these coarse precipitated phases can also easily cause propagation of cracks.

To sum up, the introduction of micron-sized TiB_2 particles by the external method do have a positive effect, such as improving the densification and slightly improving the mechanical properties. However, there is space for further improvement. The reason for this is that the micron-sized TiB_2 particles introduced by the external method are too large to achieve the effect of fine grain strengthening, and the effect of Orowan strengthening and load bearing is also minimal due to insufficient additions. Besides, most of the particles

added are irregular in shape, which may cause stress concentration. Therefore, the use of nano-sized particles TiB_2 should be the focus of subsequent experiments, and the synergistic effect of TiB_2 and Sc, Zr micro-alloyed Al matrix composites can also be further studied.

Supplementary Materials: The following supporting information can be downloaded at: <https://www.mdpi.com/article/10.3390/ma16052112/s1>, Figure S1: Particle size distribution of $\text{TiB}_2/\text{AlZnMgCu}(\text{Sc,Zr})$ powder, D10, D50 and D90 are 14.73 μm , 27.37 μm and 43.91 μm , respectively; Figure S2: The horizontal samples formed by SLM (a) upper surface and (b) side surface; Figure S3: Diagram of horizontal tensile bar (a) schematic diagram (mm) and (b) real sample; Figure S4: Pore size distribution of $\text{TiB}_2/\text{AlZnMgCu}(\text{Sc,Zr})$ fabricated by SLM; Figure S5: Distribution of micropores in $\text{TiB}_2/\text{AlZnMgCu}(\text{Sc,Zr})$ composite samples; Figure S6: Phase analysis of $\text{AlZnMgCu}(\text{Sc,Zr})$ alloy and $\text{TiB}_2/\text{AlZnMgCu}(\text{Sc,Zr})$ composite before and after heat treatment; Figure S7: HAADF image of the interface between micron- TiB_2 particle and Al matrix in SLM-fabricated $\text{TiB}_2/\text{AlZnMgCu}(\text{Sc,Zr})$ composite (a) in relatively low magnification, (b) in relatively high magnification and (c) EDS liner scanning; Figure S8: Comparison of mechanical properties of $\text{AlZnMgCu}(\text{Sc,Zr})$ and $\text{TiB}_2/\text{AlZnMgCu}(\text{Sc,Zr})$ composite before and after heat treatment; Figure S9: Tensile engineering stress-strain curves of $\text{TiB}_2/\text{AlZnMgCu}(\text{Sc,Zr})$ composite and $\text{AlZnMgCu}(\text{Sc,Zr})$ alloy samples before and after heat treatment.

Author Contributions: Conceptualization, P.Y. and Y.Z.; Methodology, P.Y. and Y.Z.; Validation, P.Y. and W.P.; Investigation, P.Y. and S.S.; Writing—original draft, P.Y.; Writing—review and editing, Y.Z., Y.L. and Z.L.; Supervision, Y.Z. All authors have read and agreed to the published version of the manuscript.

Funding: This research received no external funding.

Institutional Review Board Statement: Not applicable.

Informed Consent Statement: Not applicable.

Data Availability Statement: Data are contained within the article.

Acknowledgments: The financial support by GRINM Metal Composites Technology Co., Ltd. and research platform support by National Engineering & Technology Research Center for Non-ferrous Metal Matrix Composites, GRINM Group Co., Ltd. are greatly acknowledged.

Conflicts of Interest: The authors declare no conflict of interest.

References

1. Sadeghi, B.; Cavaliere, P.; Pruncu, C.I.; Balog, M.; Marques de Castro, M.; Chahal, R. Architectural design of advanced aluminum matrix composites: A review of recent developments. *Crit. Rev. Solid State* **2022**, *35*, 1–71. [[CrossRef](#)]
2. Zhang, X.; Chen, Y.; Hu, J. Recent advances in the development of aerospace materials. *Prog. Aerosp. Sci.* **2018**, *97*, 22–34. [[CrossRef](#)]
3. Tan, C.; Weng, F.; Sui, S.; Chew, Y.; Bi, G. Progress and perspectives in laser additive manufacturing of key aeroengine materials. *Int. J. Mach. Tools Manuf.* **2021**, *170*, 103804. [[CrossRef](#)]
4. Kontis, P.; Chauvet, E.; Peng, Z.; He, J.; da Silva, A.K.; Raabe, D.; Tassin, C.; Blandin, J.-J.; Abed, S.; Dendievel, R.; et al. Atomic-scale grain boundary engineering to overcome hot-cracking in additively-manufactured superalloys. *Acta Mater.* **2019**, *177*, 209–221. [[CrossRef](#)]
5. Herzog, D.; Seyda, V.; Wycisk, E.; Emmelmann, C. Additive Manufacturing of Metals. *Acta Mater.* **2016**, *117*, 371–392.
6. Hooper, P.A. Melt pool temperature and cooling rates in laser powder bed fusion. *Addit. Manuf.* **2018**, *22*, 548–559. [[CrossRef](#)]
7. Kotadia, H.R.; Gibbons, G.; Das, A.; Howes, P.D. A review of Laser Powder Bed Fusion Additive Manufacturing of aluminium alloys: Microstructure and properties. *Addit. Manuf.* **2021**, *46*, 102155. [[CrossRef](#)]
8. Fu, J.; Li, H.; Song, X.; Fu, M.W. Multi-scale defects in powder-based additively manufactured metals and alloys. *J. Mater. Sci. Technol.* **2022**, *122*, 165–199. [[CrossRef](#)]
9. Aboulkhair, N.T.; Simonelli, M.; Parry, L.; Ashcroft, I.; Tuck, C.; Hague, R. 3D Printing of Aluminium Alloys: Additive Manufacturing of Aluminium Alloys Using Selective Laser Melting. *Prog. Mater. Sci.* **2019**, *106*, 100578.
10. Dursun, T.; Soutis, C. Recent developments in advanced aircraft aluminium alloys. *Mater. Des.* **2014**, *56*, 862–871. [[CrossRef](#)]
11. Michi, R.A.; Plotkowski, A.; Shyam, A.; Dehoff, R.R.; Babu, S.S. Towards high-temperature applications of aluminium alloys enabled by additive manufacturing. *Int. Mater. Rev.* **2022**, *67*, 298–345. [[CrossRef](#)]
12. Priya, P.; Johnson, D.R.; Krane, M.J.M. Precipitation during cooling of 7XXX aluminum alloys. *Comput. Mater. Sci.* **2017**, *139*, 273–284. [[CrossRef](#)]

13. Sha, G.; Wang, Y.B.; Liao, X.Z.; Duan, Z.C.; Ringer, S.P.; Langdon, T.G. Influence of Equal-Channel Angular Pressing on Pre-cipitation in an Al–Zn–Mg–Cu Alloy. *Acta Mater.* **2009**, *57*, 3123–3132. [[CrossRef](#)]
14. Pauly, S.; Wang, P.; Kühn, U.; Kosiba, K. Experimental determination of cooling rates in selectively laser-melted eutectic Al–33Cu. *Addit. Manuf.* **2018**, *22*, 753–757. [[CrossRef](#)]
15. Martin, J.H.; Yahata, B.D.; Hundley, J.M.; Mayer, J.A.; Schaedler, T.A.; Pollock, T.M. 3D printing of high-strength aluminium alloys. *Nature* **2017**, *549*, 365–369. [[CrossRef](#)]
16. Li, L.; Li, R.; Yuan, T.; Chen, C.; Zhang, Z.; Li, X. Microstructures and Tensile Properties of a Selective Laser Melted Al–Zn–Mg–Cu (Al7075) Alloy by Si and Zr Microalloying. *Mater. Sci. Eng. A* **2020**, *787*, 139492. [[CrossRef](#)]
17. Zhou, S.Y.; Su, Y.; Wang, H.; Enz, J.; Ebel, T.; Yan, M. Selective Laser Melting Additive Manufacturing of 7XXX Series Al–Zn–Mg–Cu Alloy: Cracking Elimination by Co-Incorporation of Si and TiB₂. *Addit. Manuf.* **2020**, *36*, 101458. [[CrossRef](#)]
18. Zhu, Z.; Ng, F.L.; Seet, H.L.; Lu, W.; Liebscher, C.H.; Rao, Z.; Raabe, D.; Mui Ling Nai, S. Superior mechanical properties of a selective-laser-melted AlZnMgCuScZr alloy enabled by a tunable hierarchical microstructure and dual-nanoprecipitation. *Mater. Today* **2021**, *52*, 90–101. [[CrossRef](#)]
19. Li, X.P.; Ji, G.; Chen, Z.; Addad, A.; Wu, Y.; Wang, H.W.; Vleugels, J.; Van Humbeeck, J.; Kruth, J.P. Selective Laser Melting of nano-TiB₂ Decorated AlSi10Mg Alloy with High Fracture Strength and Ductility. *Acta Mater.* **2017**, *129*, 183–193. [[CrossRef](#)]
20. Wang, H.; Gu, D. Nanometric TiC reinforced AlSi10Mg nanocomposites: Powder preparation by high-energy ball milling and consolidation by selective laser melting. *J. Compos. Mater.* **2014**, *49*, 1639–1651. [[CrossRef](#)]
21. Pan, W.; Zhai, Z.; Liu, Y.; Liang, B.; Liang, Z.; Zhang, Y. Research on Microstructure and Cracking Behavior of Al–6.2Zn–2Mg–xSc–xZr Alloy Fabricated by Selective Laser Melting. *Crystals* **2022**, *12*, 1500. [[CrossRef](#)]
22. Gu, D.; Yang, Y.; Xi, L.; Yang, J.; Xia, M. Laser absorption behavior of randomly packed powder-bed during selective laser melting of SiC and TiB₂ reinforced Al matrix composites. *Opt. Laser Technol.* **2019**, *119*, 105600. [[CrossRef](#)]
23. Qu, M.; Guo, Q.; Escano, L.I.; Nabaa, A.; Hojjatzadeh, S.M.H.; Young, Z.A.; Chen, L. Controlling Process Instability for Defect Lean Metal Additive Manufacturing. *Nat. Commun.* **2022**, *13*, 1079. [[CrossRef](#)] [[PubMed](#)]
24. Shirvanimoghaddam, K.; Hamim, S.U.; Karbalaee Akbari, M.; Fakhrhoseini, S.M.; Khayyam, H.; Pakseresht, A.H.; Ghasali, E.; Zabet, M.; Munir, K.S.; Jia, S.; et al. Carbon fiber reinforced metal matrix composites: Fabrication processes and properties. *Compos. Part A Appl. Sci. Manuf.* **2017**, *92*, 70–96. [[CrossRef](#)]
25. Geng, J.; Li, Y.; Xiao, H.; Wang, Z.; Wang, M.; Chen, D.; Wang, H. Deformation-induced ultrafine grains near fatigue crack tip and correlative fatigue damage in Al matrix composite. *Scr. Mater.* **2021**, *193*, 49–54. [[CrossRef](#)]
26. Shao, H.; Liu, T.; Zhang, K.; Zhang, C.; Jiang, S.; Xiong, Z.; Liao, W. Preparation of Ti₃AlC₂ matrix composites by selective laser melting combined with pressureless sintering. *Adv. Appl. Ceram.* **2020**, *119*, 158–165. [[CrossRef](#)]
27. Ghosh, S.K.; Saha, P.; Kishore, S. Influence of Size and Volume Fraction of SiC Particulates On Properties of Ex Situ Reinforced Al–4.5Cu–3Mg Metal Matrix Composite Prepared by Direct Metal Laser Sintering Process. *Mater. Sci. Eng. A* **2010**, *527*, 4694–4701. [[CrossRef](#)]
28. Xie, J.; Chen, Y.; Yin, L.; Zhang, T.; Wang, S.; Wang, L. Microstructure and mechanical properties of ultrasonic spot welding TiNi/Ti6Al4V dissimilar materials using pure Al coating. *J. Manuf. Process.* **2021**, *64*, 473–480. [[CrossRef](#)]
29. Meng, C.; Cui, H.-C.; Lu, F.-G.; Tang, X.-H. Evolution behavior of TiB₂ particles during laser welding on aluminum metal matrix composites reinforced with particles. *Trans. Nonferrous Met. Soc.* **2013**, *23*, 1543–1548. [[CrossRef](#)]
30. Zhang, L.-L.; Jiang, H.-X.; He, J.; Zhao, J.-Z. Kinetic behaviour of TiB₂ particles in Al melt and their effect on grain refinement of aluminium alloys. *Trans. Nonferrous Met. Soc.* **2020**, *30*, 2035–2044. [[CrossRef](#)]
31. Xi, L.; Kaban, I.; Nowak, R.; Korpała, B.; Bruzda, G.; Sobczak, N.; Mattern, N.; Eckert, J. High-temperature wetting and interfacial interaction between liquid Al and TiB₂ ceramic. *J. Mater. Sci.* **2015**, *50*, 2682–2690. [[CrossRef](#)]
32. Ma, Y.; Addad, A.; Ji, G.; Zhang, M.; Lefebvre, W.; Chen, Z.; Ji, V. Atomic-Scale Investigation of the Interface Precipitation in a TiB₂ Nanoparticles Reinforced Al–Zn–Mg–Cu Matrix Composite. *Acta Mater.* **2020**, *185*, 287–299. [[CrossRef](#)]
33. Ma, Y.; Chen, H.; Zhang, M.; Addad, A.; Kong, Y.; Lezaack, M.B.; Gan, W.; Chen, Z.; Ji, G. Break through the strength-ductility trade-off dilemma in aluminum matrix composites via precipitation-assisted interface tailoring. *Acta Mater.* **2023**, *242*, 118470. [[CrossRef](#)]
34. Su, Y.; Zhu, J.; Long, X.; Zhao, L.; Chen, C.; Liu, C. Statistical effects of pore features on mechanical properties and fracture behaviors of heterogeneous random porous materials by phase-field modeling. *Int. J. Solids Struct.* **2023**, *264*, 112098. [[CrossRef](#)]
35. Wang, Z.; Lin, X.; Kang, N.; Hu, Y.; Chen, J.; Huang, W. Strength-ductility synergy of selective laser melted Al–Mg–Sc–Zr alloy with a heterogeneous grain structure. *Addit. Manuf.* **2020**, *34*, 101260. [[CrossRef](#)]
36. Wang, Z.; Lin, X.; Kang, N.; Wang, Y.; Yu, X.; Tan, H.; Yang, H.; Huang, W. Making Selective-Laser-Melted High-Strength Al–Mg–Sc–Zr Alloy Tough Via Ultrafine and Heterogeneous Microstructure. *Scripta Mater.* **2021**, *203*, 114052. [[CrossRef](#)]
37. Spierings, A.B.; Dawson, K.; Heeling, T.; Uggowitzer, P.J.; Schäublin, R.; Palm, F.; Wegener, K. Microstructural features of Sc- and Zr-modified Al–Mg alloys processed by selective laser melting. *Mater. Des.* **2017**, *115*, 52–63. [[CrossRef](#)]
38. Spierings, A.B.; Dawson, K.; Voegtlin, M.; Palm, F.; Uggowitzer, P.J. Microstructure and mechanical properties of as-processed scandium-modified aluminium using selective laser melting. *CIRP Ann.* **2016**, *65*, 213–216. [[CrossRef](#)]
39. Costa, S.; Puga, H.; Barbosa, J.; Pinto, A.M.P. The Effect of Sc Additions on the Microstructure and Age Hardening Behavior of as Cast Al–Sc Alloys. *Mater. Des.* **2012**, *42*, 347–352. [[CrossRef](#)]

40. Knipling, K.E.; Karnesky, R.A.; Lee, C.P.; Dunand, D.C.; Seidman, D.N. Precipitation evolution in Al–0.1Sc, Al–0.1Zr and Al–0.1Sc–0.1Zr (at.%) alloys during isochronal aging. *Acta Mater.* **2010**, *58*, 5184–5195. [[CrossRef](#)]
41. Wang, J.; Liu, T.; Luo, L.; Cai, X.; Wang, B.; Zhao, J.; Cheng, Z.; Wang, L.; Su, Y.; Xue, X.; et al. Selective Laser Melting of High-Strength TiB₂/AlMgScZr Composites: Microstructure, Tensile Deformation Behavior, and Mechanical Properties. *J. Mater. Res. Technol.* **2022**, *16*, 786–800. [[CrossRef](#)]
42. Yang, H.; Cai, Z.; Zhang, Q.; Shao, Y.; Dong, B.; Xuan, Q.; Qiu, F. Comparison of the Effects of Mg and Zn on the Interface Mismatch and Compression Properties of 50 Vol% TiB₂/Al Composites. *Ceram. Int.* **2021**, *47*, 22121–22129. [[CrossRef](#)]
43. Xue, G.; Ke, L.; Zhu, H.; Liao, H.; Zhu, J.; Zeng, X. Influence of processing parameters on selective laser melted SiCp/AlSi10Mg composites: Densification, microstructure and mechanical properties. *Mater. Sci. Eng. A* **2019**, *764*. [[CrossRef](#)]
44. Yi, J.; Zhang, X.; Rao, J.H.; Xiao, J.; Jiang, Y. In-Situ Chemical Reaction Mechanism and Non-Equilibrium Microstructural Evolution of (TiB₂ + TiC)/AlSi10Mg Composites Prepared by SLM-CS Processing. *J. Alloy. Compd.* **2021**, *857*, 157553. [[CrossRef](#)]
45. Gao, C.; Liu, Z.; Xiao, Z.; Zhang, W.; Wong, K.; Akbarzadeh, A.H. Effect of heat treatment on SLM-fabricated TiN/AlSi10Mg composites: Microstructural evolution and mechanical properties. *J. Alloy. Compd.* **2021**, *853*, 156722. [[CrossRef](#)]
46. Xi, X.; Chen, B.; Tan, C.; Song, X.; Feng, J. Microstructure and mechanical properties of SiC reinforced AlSi10Mg composites fabricated by laser metal deposition. *J. Manuf. Process.* **2020**, *58*, 763–774. [[CrossRef](#)]
47. Biffi, C.A.; Bassani, P.; Fiochi, J.; Albu, M.; Tuissi, A. Selective Laser Melting of AlCu-TiB₂ Alloy Using Pulsed Wave Laser Emission Mode: Processability, Microstructure and Mechanical Properties. *Mater. Des.* **2021**, *204*, 109628. [[CrossRef](#)]
48. Oliveira de Menezes, J.T.; Castrodeza, E.M.; Casati, R. Effect of build orientation on fracture and tensile behavior of A357 Al alloy processed by Selective Laser Melting. *Mater. Sci. Eng. A* **2019**, *766*, 138392. [[CrossRef](#)]

Disclaimer/Publisher’s Note: The statements, opinions and data contained in all publications are solely those of the individual author(s) and contributor(s) and not of MDPI and/or the editor(s). MDPI and/or the editor(s) disclaim responsibility for any injury to people or property resulting from any ideas, methods, instructions or products referred to in the content.